FEDSM2022-86684

MODELING AND COMPUTATION OF BATOID SWIMMING INSPIRED PITCHING IMPACT ON WAKE STRUCTURE AND HYDRODYNAMIC PERFORMANCE

Alec Menzer

Department of Mechanical and Aerospace Engineering, University of Virginia Charlottesville, VA

Yuchen Gong

Department of Mechanical and Aerospace Engineering, University of Virginia Charlottesville, VA

Chengyu Li

Department of Mechanical Engineering, Villanova University Villanova, PA

Haibo Dong

Department of Mechanical and Aerospace Engineering, University of Virginia Charlottesville, VA

Frank Fish

Department of Biology West Chester University West Chester, PA

ABSTRACT

Through direction numerical simulation (DNS) of a model manta ray body, pectoral fin scaled pitching effect on hydrodynamic performance and wake is investigated. The manta ray model is derived from high-speed video of manta ray swimming with motion of the model prescribed to match the actual manta ray. Rotation angles of the model skeletal joints is altered to scale the pitching. This results in four manta ray models with different pectoral fin pitching ratios. The models are simulated using an in-house developed immersed boundary method-based numerical solver. Notable discrepancies in thrust production during the downstroke are observed, with the $\theta_R = 1.0$ case producing instantaneous thrust peak that is 19% higher than the $\theta_R = 0.72$ model. Cycle averaged thrust is highest for the $\theta_R = 0.72$ model case, however, which can be attributed to extended reverse thrust for the $\theta_R = 1.0$ model. Through analysis of the near-body wake structures produced during the downstroke, late leading-edge vortex (LEV) formation is discovered to be primarily responsible for the detrimental reverse thrust seen for the $\theta_R = 1.0$ model. Surface pressure contours confirm this finding. Meanwhile the upstroke possesses less pronounced force production.

Keywords: direct numerical simulation, wakes, computational fluid dynamics, hydrodynamics

NOMENCLATURE

BL	Model manta ray body length
S	Model manta ray span length
A	Model pectoral fin flapping amplitude
$ heta_f$	Pectoral fin pitching angle (°)
$\hat{ heta}_M$	Maximum pectoral fin pitching at $s/S = 0.66$
$ heta_R$	Pectoral fin pitching ratio
f	Pectoral fin flapping frequency
T	Period of cycle of motion
ρ	Density of fluid
v	Kinematic viscosity
U_{∞}	Incoming flow velocity
Re	Reynolds number
St	Strouhal number
C_T , C_{PW}	Instantaneous thrust, power coefficient
$\overline{C_T}$, $\overline{C_{PW}}$,	Cycle averaged thrust, power coefficient
R	Tow drag resistance

1. INTRODUCTION

Taking inspiration from biological locomotion to produce robots that mimic their natural counterparts has proved an effective method for designing efficient robots. A distinct characteristic of batoids and batoid swimming is the dorsoventrally flattened body profile and undulatory or oscillatory behavior of the pectoral fins for means of propulsion [1]. Manta rays possess flexible pectoral fins that exhibits spatial and temporal variations of bending and pitching throughout the oscillatory flapping motion especially in the distal regions of the fin [2]. The combination of pitching and rolling with spatial variations in twist angle resulting in a bio-inspired flapping foil has been investigated. The twisting results in higher effective pitching angles along the span of the elliptic shaped plates. It was shown that moderate twisting results in an increase in propulsive efficiency despite lower thrust due to power consumption reduction [3]. Optimization of spanwise bending and twisting has also shown that twisting increases efficiency [4]. Further characterization of performance and wake structures has been performed for canonical stationary and bio-inspired flapping plates without deformation [5,6]. Yaw control 0l of pectoral finlike flapping plates, through introduction of control of flapping, has even been studied [7]. However, little is still known about how these kinematics factor into hydrodynamic performance when incorporated into complex biological models.

Recent work has analyzed how chordwise deformations modeled by a travelling wave impacts cownose ray swimming performance. LEV induced suction was deemed significant in the cownose ray force production. Increased chordwise deformations were found to lower force production but correspondingly directed more of the produced force in the streamwise direction [8]. In depth characterization of manta pectoral fin motion and swimming efficiency [2] as well as maneuvering performance [9] is prevalent yet investigation of the role of pectoral fin pitching in hydrodynamic performance and wake topology of manta swimming is minimal.

The goal of this research is to characterize the role of pectoral fin pitching in propulsive manta ray swimming. This will result in an improved understanding of the mechanisms that mantas utilize in efficient swimming which has applications in manta-inspired robotic locomotion.

2. MATERIALS AND METHODS

2.1. 3D manta ray model kinematics

The current work utilizes a digital manta ray model constructed using 3D modeling and animation software. The model is composed of a body skin bound to a skeleton. Motion of the body skin is dictated by motion of the skeletal joints which originates from underwater videos of manta ray swimming captured by Dr. Frank Fish. Using video perspective views skeletal joint x,y, and z rotations are altered so that the model manta ray motion pectoral fin motion matches that of the real manta ray [2]. This joint-based method has been used for reconstructing swimming motion [2,10]. Figure 1 illustrates the pectoral fin motion during the downstroke of the flapping motion with the geometric parameters θ_f , A, BL, and S defined.

Scaling factors are applied to the each of the joint's x-rotations to reduce the fin pitching angle of the model. The model with no scaling retains the extreme pectoral fin pitching observed by the real manta ray while each model constructed with scaled pitching motion possesses less extreme pectoral fin pitching. θ_M is defined as the maximum downstroke pitching angle at the s/S = 0.66 chord line. The ratio of θ_M for a model with scaled pitching and θ_M for the model with unscaled pitching defines the pitching ratio θ_R .

Figure 2 shows how the instantaneous pectoral fin pitching angle θ_f for each model at s/S=0.66 varies during a full cycle of motion. For the unscaled model θ_M at s/S=0.66 is about 40°, however, θ_M increases further along the span reaching up to 80° near the fin tip.

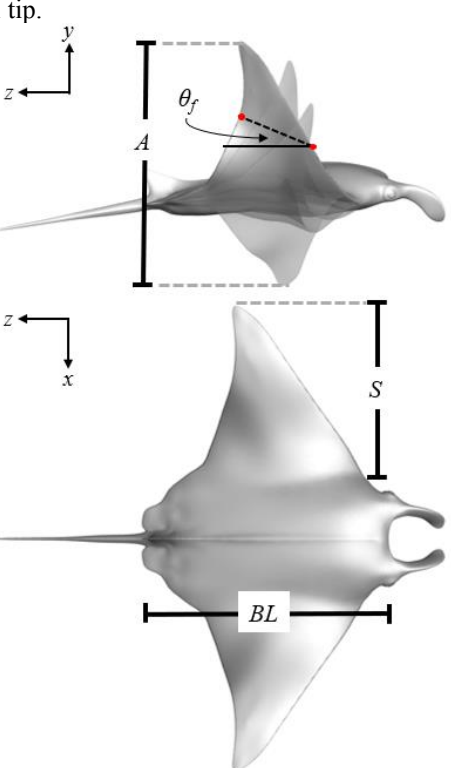


FIGURE 1: SIDE AND OVERHEAD VIEWS OF THE MANTA RAY MODEL ILLUSTRATING GEOMETRIC PARAMETERS

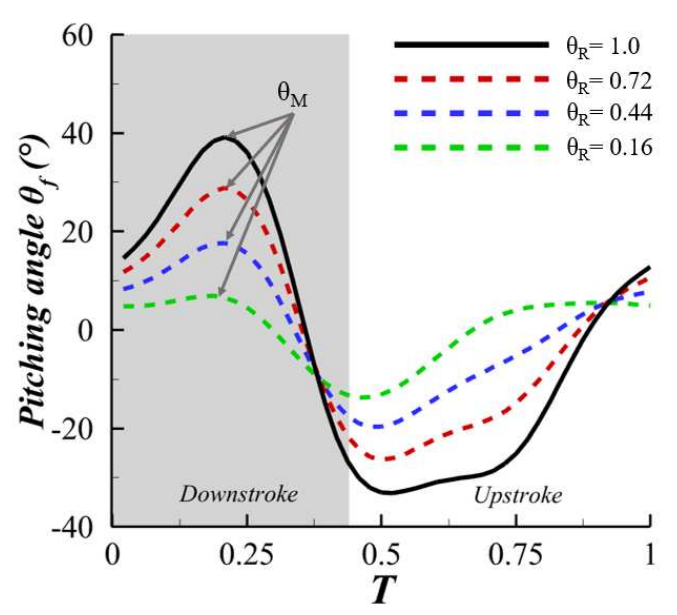


FIGURE 2: COMPARISON OF INSTANTANEOUS PITCHING ANGLE θ_f AT s/S=0.66 FOR EACH CASE

2.2. Numerical method and simulation setup

The governing fluids equations solved in this work and the incompressible Navier-Stokes equations,

$$\frac{\partial u_i}{\partial x_i} = 0; \quad \frac{\partial u_i}{\partial t} + \frac{\partial u_i u_j}{\partial x_j} = -\frac{\partial p}{\partial x_i} + \frac{1}{Re} \frac{\partial^2 u_i}{\partial x_i \partial x_j} \tag{1}$$

where u_i are the velocity components, p is the pressure, and Re is the Reynolds number. The equations are nondimensionalized with the appropriate length and velocity scales.

An in-house finite-difference based Cartesian-grid sharp-interface immersed-boundary-method direction numerical simulation solver is employed to solve the above equations. This solver has been validated and applied to various relevant biological flows such as flapping of canonical shapes [11-13] and complex bio-inspired geometries [10,14-17].

In this study, the non-dimensional parameters of Reynolds number and Strouhal number are defined as follows.

Re
$$=\frac{U_{\infty}BL}{v}$$
; $St = \frac{Af}{U_{\infty}}$ (2)

Values for the simulation parameters can be found in Table 1.

TABLE 1: Summary of parameters in this study

U_{∞}	f	BL	Α	Re	St
1	1	1	1	1200	1

The computational domain has dimensions of 20BL x 20BL x 20 BL. A Cartesian grid configuration with a stretching grid is used. The spacing of the cells in all 3 spatial directions within the densest region is $\Delta = 0.0085 \, BL$ with a semi dense grid region just downstream from the densest region. Grid density of the current fine-ness has been proven sufficient for the simulations. To achieve this density in the near-field regions, adaptive mesh refinement (AMR) techniques are utilized. Two block-structured-mesh bodies are implemented. A large parent

block captures far-field wake structures downstream of the model while a smaller block with boundaries closer the model enhances grid density in the near-field. For maximal efficiency of the AMR algorithm the incoming flow velocity is set to be in the z-direction. A homogeneous Neumann boundary condition is used for the pressure at all boundaries.

Figure 3 illustrates the computational grid including location and relative size of the AMR blocks. For the base mesh and AMR blocks, every 4th grid point is shown to more clearly illustrates grid locations. More details related to the AMR algorithm can be found in Ref. [18].

To quantify the hydrodynamic performance of the simulated models, *Thrust* is considered as pressure force opposite to the z-direction, *Drag* is considered as shear force along the z-direction, and *Lift* as pressure force in the y-direction. Force/power coefficients and efficiency are defined as follows:

$$C_T = \frac{Thrust}{\frac{1}{2}\rho U_{\infty}^2 BL}, C_{PW} = \frac{Power}{\frac{1}{2}\rho U_{\infty}^3 BL}, \eta = \frac{\overline{C_T} + R}{\overline{C_{PW}}}.$$
 (3)

where the flow and geometric parameters are as defined previously. R is defined as the C_D of the model with no fin flapping or pitching motion. For the current model R = 0.097.

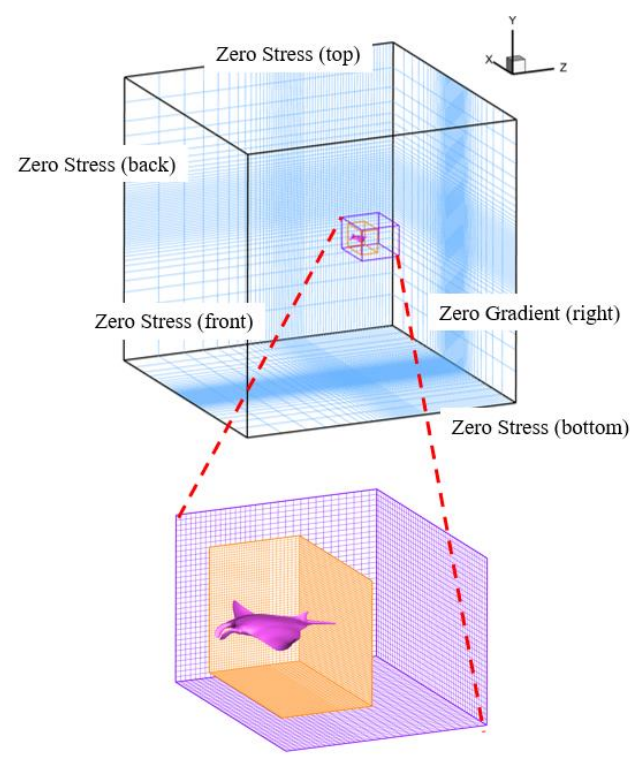


FIGURE 3: COMPUTATIONAL DOMAIN SPECIFYING BOUNDARY CONDITIONS AND RELATIVE LOCATIONS OF AMR BLOCKS

3. RESULTS AND DISCUSSION

This section compares the force production and near-body wake topology for the four cases. For each case simulations were performed for 4 cycles of motion to ensure periodicity in the force production by the models.

3.1. Hydrodynamic performance

In this subsection the effect of pitching ratio on the force production and efficiency is discussed. First the instantaneous thrust coefficients will be examined. In Figure 4 the instantaneous thrust force history for each of the cases is displayed. With lower pitching ratio peak thrust achieved during the cycle of motion decreases significantly. For $\theta_R = 1.0 C_T =$ 0.986 is achieved while peak C_T is 15% lower (0.834) for θ_R = 0.72, 34% lower (0.650) for $\theta_R = 0.44$, and 71% lower (0.286) for $\theta_R = 0.16$. Notably the peak thrust for each case is achieved exclusively during the downstroke motion. This can be attributed to both the increased pitch angles during the downstroke and the asymmetric flapping of the model. Higher pitching allows for a greater portion of the hydrodynamic force produced by the fin to be directed in the steam-wise direction. In addition, the downstroke occurs faster than the upstroke further increasing force production. As for the upstroke, the 'double peak' feature of the instantaneous thrust is consistent across all cases with each respective peak occurring at the same time during the upstroke. Additionally, the peak instantaneous thrust production occurs earlier in the downstroke as the pitching ratio is decreased. For the θ_R = 0.16, 0.44, 0.72, and 1.0 cases the peak thrust occurs at t/T=3.15, 3.21, 3.28, and 3.31, respectively.

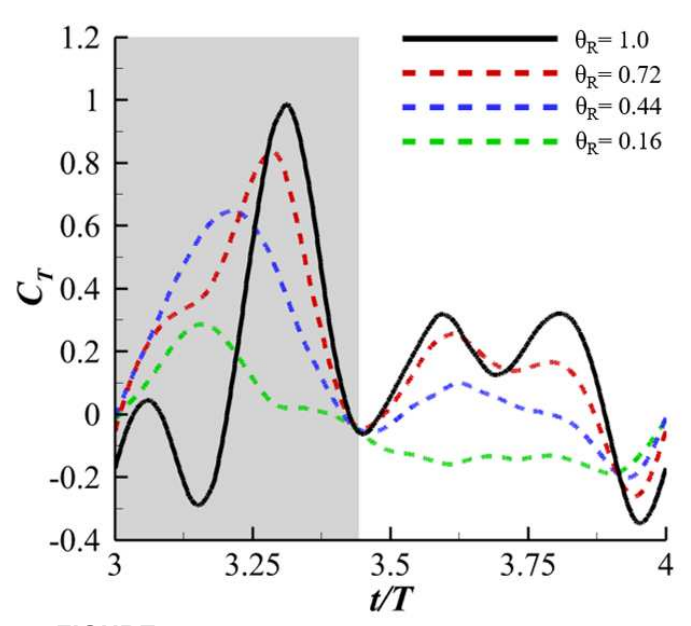


FIGURE 4: INSTANTANEOUS THRUST COEFFICIENT FOR ALL CASES DURING 1 CYCLE OF MOTION

Cycle averaged coefficient values and efficiency are displayed in Table 2. Despite the $\theta_R = 1.0$ case having the highest peak instantaneous C_T the $\theta_R = 0.72$ model produced a higher cycle averaged thrust $\overline{C_T}$.

TABLE 2: CYCLE AVERAGED THRUST/POWER COEFFICIENTS AND EFFICIENCY

θ_R	1.0	0.72	0.44	0.16
$\overline{C_T}$.	0.156	0.21	0.14	-0.03
$\overline{C_{PW}}$.	1.30	1.34	1.57	1.89
η	19.6%	22.8%	15.1%	

Observe in Figure 4 the reverse thrust produced by the θ_R = 1.0 model. This only occurs for the θ_R = 1.0 case and lasts until t/T = 3.20 which is detrimental to the cycle averaged value. In comparison the θ_R = 0.72 model continually produces forward thrust throughout the entirety of the downstroke. Also worth noting is the discrepancy in shape of the downstroke C_T peak for each case. As the pitching ratio is lowered the 'sharpness' of the downstroke thrust peak is decreased considerably, as such, models with moderately lower pitching ratio more consistently produce forward thrust.

This C_T discrepancy, in tandem with the small difference in cycle average power consumption $\overline{C_{PW}}$, results in the $\theta_R = 0.72$ model exhibiting the highest efficiency. It should be noted that due to the $\theta_R = 0.16$ model producing reverse thrust over the cycle average, no η calculation can be made. The trend observed in cycle averaged C_T and η is like that observed in a study of twisting amplitudes in low aspect ratio pitching rolling plates [3] and a cownose ray inspired model [5] and demonstrates that a balance between increased power consumption and thrust production is reached at moderate pitching angles. Further, the thrust produced by the manta models during the downstroke motion appears to be crucial in maximizing the cycle averaged thrust. Observations of wake structure formation during this period are made in the subsequent section.

3.2: Near-body wake structure formation

To compare the wakes generated by the models, perspective views of iso-surfaces visualized by Q-criterion value of 120 are shown in Figure 5. At the time shown, t/T=3.19, the pectoral fin for each model has completed just less than half the downstroke motion. In these figures the difference between the pitching angles between the cases is apparent. In Figure 5(a), corresponding to the $\theta_R=1.0$ case, the tip of the fin has a nearly vertical orientation whereas in Figure 5(d), representing $\theta_R=0.16$ case, the fin exhibits little rotation.

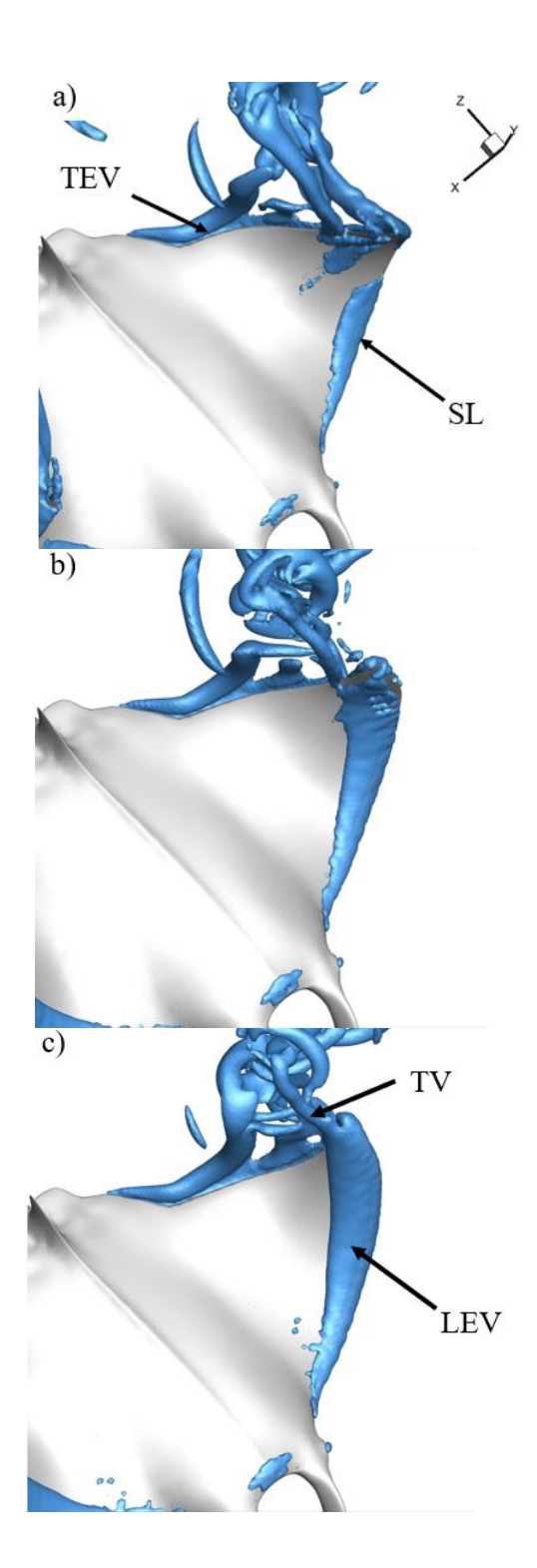




FIGURE 5: NEAR BODY WAKE STRUCTURE FORMATIONS AT t/T=3.19 FOR (a) $\theta_R=1.0$ (b) $\theta_R=0.72$ (c) $\theta_R=0.44$ (d) $\theta_R=0.16$.

The leading-edge vortex (LEV), trailing-edge vortex (TEV) and preliminary tip vortex (TV) structures are observed near the body with the LEV structures presenting significant differences between the models. For the θ_R = 1.0 case, shown in Figure (a), practically no shear layer (SL) formation is even observed despite the fin completing half of the downstroke. In contrast the θ_R = 0.72 case in Figure (b) demonstrates clear SL formation. Finally for the θ_R = 0.44 and 0.14 cases, shown in Figures (c,d), respectively, more fully formed LEV tubes can be seen on the fin surfaces. This indicates that altering pitching has implications for LEV formation on the fin surface as the vortex structure progresses from weak SL to fully formed LEV tubes from θ_R = 1.0 to 0.16. LEV formation is delayed by the increased pitching ratio.

In addition, TV formation is slightly different. For the higher θ_R cases no TV formation is observed whereas for the $\theta_R=0.44$ and $\theta_R=0.16$ cases the TV can be seen early the early stages of formation. The TV extends vertically from the fin surface appearing as an extension of the formed LEV tubes. The TV for $\theta_R=0.16$ model is larger in appearance than the TV for the $\theta_R=0.44$ model. Finally, TEV tube structures, which form because of the rolling up of the trailing-edge shear layer (TESL) on the lower surface of the fin, can be observed just behind the fin in Figure 5(a). This tube-like structure is consistent across each of the cases.

Surface pressure contour plots at t/T=3.19 for the cases are shown in Figure 6 to link the LEV formation observed in Figures 5 to the observed trend of hydrodynamic forces in Figure 4. Top surface C_P differences are clear with the $\theta_R=1.0$ case, shown in Figure 6(a), exhibiting weak low-pressure regions across the top fin surface and even regions of slight high pressure. In comparison the $\theta_R=0.72$ case in Figure 6(b) has a more consistent region of low pressure across the fin corresponding to the location of the leading-edge SL formation observed in Figure 5(b). In Figures 6(c,d) strong low pressure regions occupy a majority of the fin surface.

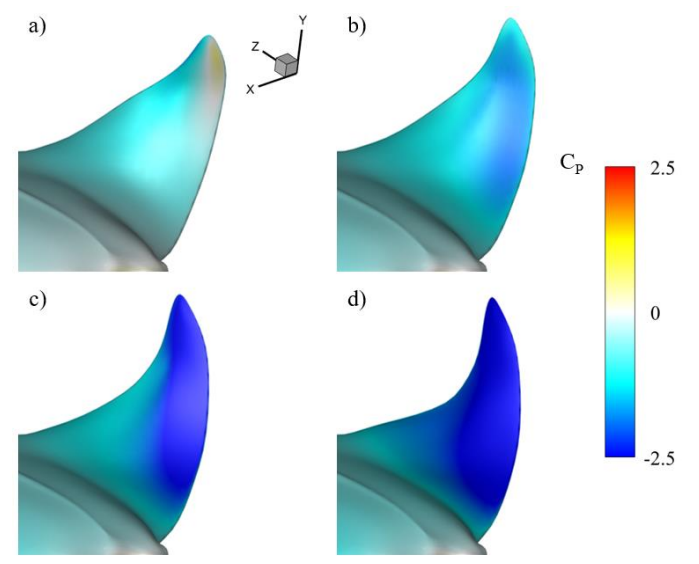


FIGURE 6: SURFACE PRESSURE C_P AT t/T=3.19 FOR (A) θ_R = 1.0 (B) θ_R = 0.72 (C) θ_R = 0.44 (D) θ_R = 0.16 MODELS

This strong suction pressure on the top surface is beneficial to force production, however, only when considering that a pitching angle is required for direction of the hydrodynamic force in the thrust direction. Thus, despite the $\theta_R = 0.16$ model having the largest low C_P region, the low pitching angle directs very little of the resulting suction force in the streamwise direction. The $\theta_R = 1.0$ model has the least robust low-pressure regions, and even features a slight region of high pressure on the top surface. This trend of low surface pressure confirms that late LEV formation contributes to the production of reverse thrust and forward thrust during the downstroke for the $\theta_R = 1.0$ and $\theta_R = 0.72$ models, respectively.

This LEV phenomenon has been documented to occur for pitching plunging plates where increase in maximum effective angle of attack correlates to stronger LEV structures and earlier vortex separation [19]. For the current manta ray models, the lower pitching ratio models exhibit lower pitching angles which corresponds to higher angles of attack.

4. CONCLUSION

In the present study direct numerical simulation of manta ray models with various pitch ratios has been conducted. The degree of pitching has significant impact on the hydrodynamic performance of the manta models. Lowering the pitching ratio to $\theta_R = 0.72$ increases cycle averaged thrust production despite the $\theta_R = 1.0$ model generating a higher instantaneous thrust coefficient. This is due to a lack of top surface suction pressure during the first half of the downstroke which is caused by delayed formation of the LEV. The associated increase in power consumption between the cases is minimal, therefore, maximal efficiency is achieved for the $\theta_R = 0.72$ case. This study has potential to improve understanding of the role of pectoral fin kinematics in manta ray propulsion. Further there exists potential applications in motivating manta inspired robots that feature some of the extreme pectoral fin deformations seen in their biological counterparts.

ACKNOWLEDGEMENTS

This research was supported by the National Science Foundation Research Traineeship (NRT) program under Grant No.1829004, ONR-MURI Grant N00014-14-1-0533, and NSF Grant CNS-1931929. Computational resources on the UVA Rivanna computing cluster were provided by the UVA Research Computing Group.

REFERENCES

- [1] Rosenberger, L.J. 2001. "Pectoral Fin Locomotion in Batoid Fishes: Undulation versus Oscillation," *The Journal of Experimental Biology*, 204, pp. 379-394.
- [2] Fish, F., Schreiber, C., Lui, G., Dong, H., Bart-Smith, H. 2016. "Hydrodynamic performance of aquatic flapping: Efficiency of underwater flight in the manta," *Aerospace*, 3,20, pp. 1-24. doi: 10.3390/aerospace3030020.
- [3] Tu,Y., Wang, J., Hu, H., Dong, H. 2020. "Twist morphing effect on propulsive performance of bioinspired pitching-rolling plates," Proceedings of AIAA Scitech Forum, Orlando, FL, January 6-10, 2020, pp.1-14. doi:10.2514/6.2020-2019.
- [4] Jia, K., Wei, M. 2021. "Optimization of Flexible Wings for Thrust and Efficiency," Proceedings AIAA Aviation Forum, August 2-6, 2021, pp. 1-14. doi: 10.2514/6.2021-2570.
- [5] Li, C., Dong, H. 2016. "Three-dimensional wake topology and propulsive performance of low-aspect-ratio pitching-rolling plates," *Physics of Fluids*, 28, 7. doi:10.1063/1.4954505
- [6] Ghias, R., Mittal, R., Dong, H., Lund, T. 2005. "Study of tip-vortex formation using large-eddy simulation," 43rd AIAA Aerospace Sciences Meeting and Exhibit, Reno, Nevada, January 10-13, 2005. pp. 10853-10865. doi: 10.2514/6.2005-1280.
- [7] Narasimhan, M., Dong, H., Mittal, R., Singh, SN. 2006. "Optimal yaw regulation and trajectory control of biorobotic AUV using mechanical fins based on CFD parameterization," *Journal of Fluids Engineering*, 128, 4, pp. 687-698. doi: 10.1115/1.2201634.
- [8] Zhang, D., Huang, Q., Pan, G., Yang, L., Huang, W. 2020. "Vortex dynamics and hydrodynamic performance enhancement in batoid fish oscillatory swimming," *Journal of Fluid Mechanics*, 930, pp. A28 1-32. doi: 10.1017/jfm.2021.917.
- [9] Fish, F., Kolpas, A., Crossett, A., Moored, K., Bart-Smith, H. 2018. "Kinematics of swimming of the manta ray: Three-dimensional analysis of open-water maneuverability," *Journal of Experimental Biology*, 221, pp. 1-10. doi: 10.1242/jeb.166041.
- [10] Menzer, A., Gong, Y., Fish, F.E., Dong, H. 2022. "Bio-Inspired propulsion: Towards understanding the role of pectoral fin kinematics in manta-like swimming," *Biomimetics*, 7(2), 45. doi:10.3390/biomimetics7020045.
- [11] Dong, H., Liang, Z., Harff., M. 2009. "Optimal settings of aerodynamic performance parameters in hovering flight," *International Journal of Micro Air Vehicles*, 1(3), pp. 173-181.

- [12] Geng, B., Xue, Q., Zheng, X., Liu, G., Ren, Y., Dong, D. 2018. "The effect of wing flexibility on sound generation of flapping wings," *Bioinspiration and Biomimetics*, 1(3). doi: 10.1088/1748-3190/aa8447.
- [13] Bozkurttas, M., Dong, H., Seshadri, R., Mittal, R., Najjar, F. 2005. "Towards numerical simulation of flapping foils on fixed Cartesian grids," 43rd AIAA Aerospace Sciences Meeting and Exhibit, Reno, Nevada, January 10-13, 2005. pp. 15801-15809. doi: 10.2514/6.2005-79
- [14] Bode-Oke, AT., Zeyghami, S., Dong, H. 2017. "Aerodynamics and flow features of a damselfly in takeoff flight," *Bioinspiration and Biomimetics*, 12(5), 27. doi: 10.1088/1748-3190/aa7f52
- [15] Ren, Y., Dong, H., Deng, X., Tobalske, B. 2016. "Turning on a dime: Asymmetric vortex formation in hummingbird maneuvering flight," Physical Review of Fluids, 1(5). doi: 10.1103/aps.dfd.2015.gfm.v0088
- [16] Wang, J., Ren, Y., Dong, H. "Computational investigation of wing-body interaction and its lift enhancement effect in forward flight," *Bioinspiration and Biomimetics*, 14(4). doi: 10.1088/1748-3190/ab2208
- [17] Wang, J., Wainwright, D., Lindengren, R., Lauder, G., Dong, H. 2021. "Tuna locomotion: A computational hydrodynamic analysis of finlet fuction," *Journal of the Royal Society Interface*, 17(165), pp. 1-14. doi: 10.1098/rsif.2019.0590
- [18] Zhang, W., Pan, H., Gong, Y., Dong, H., Xi, J. 2021. "A Versatile IBM-Based AMR Method for Studying Human Snoring," Proceedings of the ASME FEDSM, August 10-12, 2021. doi:10.1115/FEDSM2021-65790.
- [19] Kang, C., Aono, H., Baik, Y.S., Bernal, L.P., Shyy, W. 2013. "Fluid Dynamics of Pitching and Plunging Flat Plate at Intermediate Reynolds Numbers," *AIAA Journal*, 51, pp. 315-329. doi: 10.2514/1.J051593.